ACS APPLIED MATERIALS & INTERFACES

www.acsami.org

Research Article

Atomic-Scale Mechanism of Grain Boundary Effects on the Magnetic and Transport Properties of Fe_3O_4 Bicrystal Films

Xiang Liu,[⊥] Mei Wu,[⊥] Ke Qu, Peng Gao,* and Wenbo Mi*

Cite This: *ACS Appl. Mater. Interfaces* 2021, 13, 6889–6896

Read Online

ACCESS | Metrics & More | Article Recommendations | Supporting Information

ABSTRACT: In strongly correlated materials, change of the local lattice configuration is expected to tune or even generate new properties otherwise in the ideal bulk materials. For highly spin-polarized materials, the spin-dependent transport is sensitive to the local magnetic structure. Here, the artificial grain boundaries (GBs) with different tilt angles are produced in Fe_3O_4 films using $SrTiO_3$ bicrystal substrates. The saturation magnetization of Fe_3O_4 bicrystal films is enhanced. The detailed atomic structural results combining with density functional theory calculations reveal that the elongated Fe_A-O bond length at GBs resulting in the reduction of charge transfer reduces the Fe_A magnetic moments, which enhances the total magnetic moments of Fe_3O_4. The in-plane rotation of the Fe_3O_4 lattice on bicrystal substrates alters the magnetization processes. Especially, the Fe_3O_4 bicrystal film with a tilt angle of 22.6° shows strong in-plane magnetic anisotropy due to the zigzag GBs. The altered magnetic anisotropy of Fe_3O_4 bicrystal films enhances the anisotropic magnetoresistance. The findings reveal the mechanism of GBs on the magnetic and transport properties and manifest that the strategy of utilizing GBs can tune the physical properties in highly spin-polarized materials.

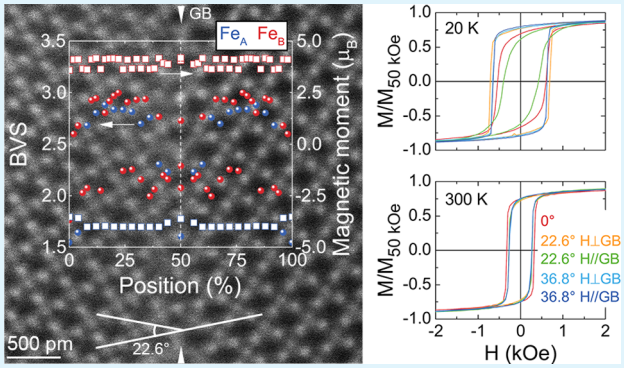

KEYWORDS: *Fe_3O_4, bicrystal, grain boundary, magnetic properties, magnetoresistance*

1. INTRODUCTION

Electron charge, spin, and orbital are coupled with the lattice structure in strongly correlated materials. Therefore, the defects in these systems stimulate the novel properties and even affect the performance of the matrix due to the change of the local structure.[1] On one hand, the defects perturb the performance of the devices. On the other hand, the defects may be beneficial to the applications and the manipulation of an ordered defect can promote the development of devices based on the nanostructure. Grain boundaries' (GBs) engineering which is constructed by artificially sintered bulk materials may serve as a general way to couple multiple order parameters at an atomic scale and exhibit unique properties.[2−5] For example, the introduction of GBs alters the magnetic field dependences of magnetoresistance (MR) because of the change of magnetization reversal processes in $La_{0.7}Sr_{0.3}MnO_3$ bicrystal films at different magnetic field directions.[6] The specific magnetic structure at GBs in $La_{2/3}Sr_{1/3}MnO_3$ bicrystal films can even result in the different chemical potential that leads to nonlinear $I-V$ characters.[7] Moreover, the electronic transport across the $La_{0.67}Ba_{0.33}MnO_3$ GB follows different mechanisms at different temperatures, which is absent in the film without GB.[8] Thanks to the controllable structure of the bicrystal, the critical current density of Josephson junctions can be tuned in $YBa_2Cu_3O_7$ films.[9,10] Similar results have been found in $Tl_2Ba_2CaCu_2O_8$ bicrystal films.[11] In $SrTiO_3$ bicrystals, the introduction of GB can lead to flexoelectric polarization at the dislocation cores.[12] Recently, Li et al. reported the atomic mechanism of spin-valve behavior in the $SrRuO_3$ bicrystal film, demonstrating a nonmagnetic layer formed at GBs.[13] Therefore, the magnetic and transport properties in ferromagnets are sensitive to the artificial GBs, especially in the materials with high spin polarization. The ability to determine the atomic arrangements of GB and signify the nature of such structural defects may advance the novel low-dimensional magnetic devices.

Magnetite (Fe_3O_4) is regarded as a candidate in spintronic devices, which attracts much attention due to its magnetic and electronic properties including ferrimagnetism and half-metallicity.[14−19] In epitaxial Fe_3O_4 films, the stacking fault generates widely distributed antiphase boundaries (APBs), where Fe_A-O-Fe_A and Fe_B−O−Fe_B are antiferromagnetic coupled.[20−23] Such abnormal magnetic interaction enlarging

Received: December 7, 2020
Accepted: January 14, 2021
Published: January 26, 2021

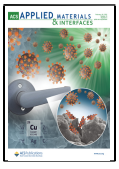

https://dx.doi.org/10.1021/acsami.0c21705
ACS Appl. Mater. Interfaces 2021, 13, 6889–6896

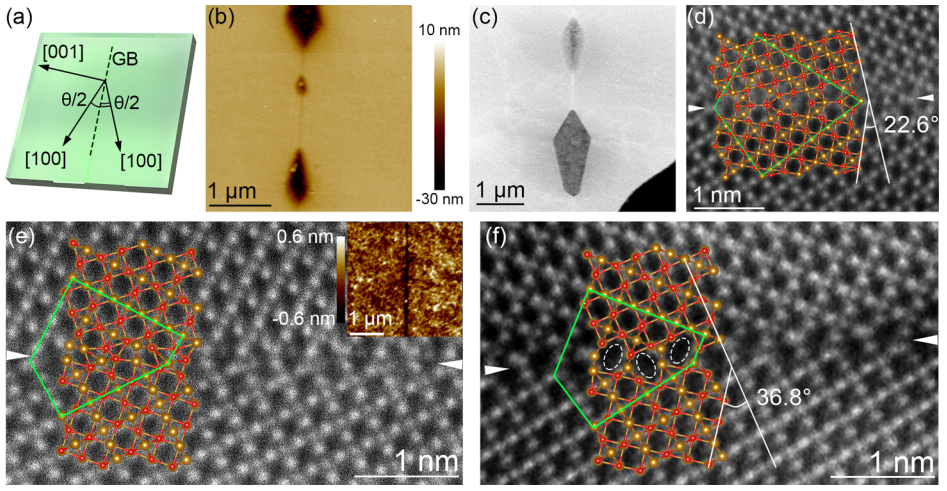

Figure 1. (a) Diagram of the $SrTiO_3$ bicrystal substrate with a tilt angle of θ. (b) Morphology and (c) low-magnification planar-view HAADF image of the Fe_3O_4 film with $\theta = 22.6°$. (d) Atomically resolved planar-view HAADF image of Fe_3O_4 GB with $\theta = 22.6°$. (e, f) Atomically resolved planar-view HAADF images of Fe_3O_4 GB with $\theta = 36.8°$. The morphology of the Fe_3O_4 film with $\theta = 36.8°$ is shown in the inset of (e). Brown and red spheres in (d–f) represent Fe and O ions. The structural units are marked by green polygons. The GBs are indicated by the white triangles.

the magnitude of MR in Fe_3O_4 films suggests the sensitivity of physical properties in Fe_3O_4 to the local lattice structure.[21,24−26] What is more, as the temperature decreases to about 120 K (T_V), Fe_3O_4 undergoes Verwey transition.[27−30] The metastable lattice structure and magnetic properties of Fe_3O_4 in the vicinity of T_V are susceptible to lattice strain, stoichiometry, and thickness.[18,31,32] When considering the introduction of GB, the producing effects of the unique lattice structure at GBs on the electronic structure, transport, magnetic properties and Verwey transition in Fe_3O_4 bicrystal films are not reported yet.

In this work, we successfully synthesized Fe_3O_4 films on $SrTiO_3$ single-crystal and bicrystal substrates and determined the atomic configurations of Fe_3O_4 at GBs. The saturation magnetizations of Fe_3O_4 bicrystal films are enhanced due to less charge transfer between elongated Fe_A-O bonds at GBs. Especially, the in-plane rotation of the Fe_3O_4 lattice in bicrystal films alters the magnetic anisotropy, which causes different magnetization processes and enhances the anisotropic MR (AMR). These works revealed the atomic-scale mechanism of GBs on the magnetic and transport properties in Fe_3O_4 bicrystal films, which may give a glimpse of defect-based spintronic devices.

2. EXPERIMENTAL AND COMPUTATIONAL DETAILS

Fe_3O_4 films on $SrTiO_3(001)$ single-crystal and bicrystal substrates with tilt angles of $\theta = 14.3°$, 22.6°, and 36.8° were fabricated by a facing-target reactive magnetron sputtering apparatus from a pair of Fe (99.99%) targets. The Ar (99.999%) and O_2 (99.999%) gas mixture with a ratio of 100:0.7 was introduced into the chamber till 0.7 Pa when the base pressure was lower than 1.0×10^{-5} Pa. A substrate temperature of 380 °C and a sputtering power of 70 W on Fe targets were used during the film deposition. The thickness of the Fe_3O_4 films with 60 nm was determined by a Dektak 6 M surface profiler. The morphology of the Fe_3O_4 films was investigated by atomic force microscopy. The structure of the Fe_3O_4 film is investigated by X-ray diffraction (XRD). The atomic structures of Fe_3O_4 at GBs were determined by high-angle annular dark-field scanning transmission electron microscopy imaging. The MR and magnetic properties of Fe_3O_4 films were measured by a Quantum Design physical properties measurement system and a magnetic properties measurement system.

The calculation models of the Fe_3O_4 bicrystal with $\theta = 22.6°$ and 36.8° were built based on the STEM results. The interfaces at GBs for $\theta = 22.6°$ and 36.8° belong to $Fe_3O_4\{510\}$ and $Fe_3O_4\{310\}$, respectively. Electronic structure calculations were performed based on the density functional theory (DFT) and generalized gradient approximation in the Vienna Ab-initio Simulation Package.[33,34] The projector-augmented-wave method was used to describe the core electrons. The exchange−correlation functional parameterization of Perdew−Burke−Ernzerhof was used. The energy cutoff of plane wave basis was set as 500 eV. A $1 \times 3 \times 1$ k-point grid centered at Γ point was set. The on-site Coulomb interaction parameter $U = 4.5$ eV and on-site exchange interaction parameter $J = 0.89$ eV were used for Fe ions as in previous works.[19,35−38] During the structure optimizations, only the positions of O ions are optimized, while the Fe ions are fixed. The structure optimizations stop after the total energy change becomes less than 10^{-5} eV and the Hellman−Feynman force of the optimized structure becomes less than 10^{-2} eV/Å.

3. RESULTS AND DISCUSSION

Figure 1a shows the definition of the tilt angle θ. The $SrTiO_3$ bicrystal substrate is divided into two parts by the GB. The angles between the GB and the $SrTiO_3[100]$ directions on both sides are $\theta/2$. Figure 1b shows the morphology of the Fe_3O_4 bicrystal film with $\theta = 22.6°$. The dark line indicates the GBs. Some voids with a depth of about 30 nm exist along the GBs. In the area away from GBs, no voids appear and the roughness of the Fe_3O_4 film is about 0.17 nm, which manifests that the voids derive from the defects in the $SrTiO_3$ bicrystal substrate. In Figure 1c, the straight light line in the low-magnification HAADF image manifests the GB and corresponding voids can be observed as well. Figure 1d presents a planar-view HAADF image of the Fe_3O_4 GBs with $\theta = 22.6°$, illustrating the symmetric arrangement of Fe_3O_4 GBs. The XRD result has shown that the Fe_3O_4 film is [001] oriented (Figure S1). Due to the superposition of O and Fe ions along $Fe_3O_4[001]$, O ions cannot be figured out from Fe ions. The structural unit of Fe_3O_4 at GBs is marked by a green polygon. It should be noted that the symmetric Fe_3O_4 lattice at GB is short-range-ordered. In Supporting Information, Figure S2a, the asymmetric Fe_3O_4 lattice suggests a zigzag GB structure. A similar result has been reported in the $YBa_2Cu_3O_7$ film on the $SrTiO_3$ bicrystal substrate with $\theta = 23°$.[10] TEM investigations

https://dx.doi.org/10.1021/acsami.0c21705
ACS Appl. Mater. Interfaces 2021, 13, 6889−6896

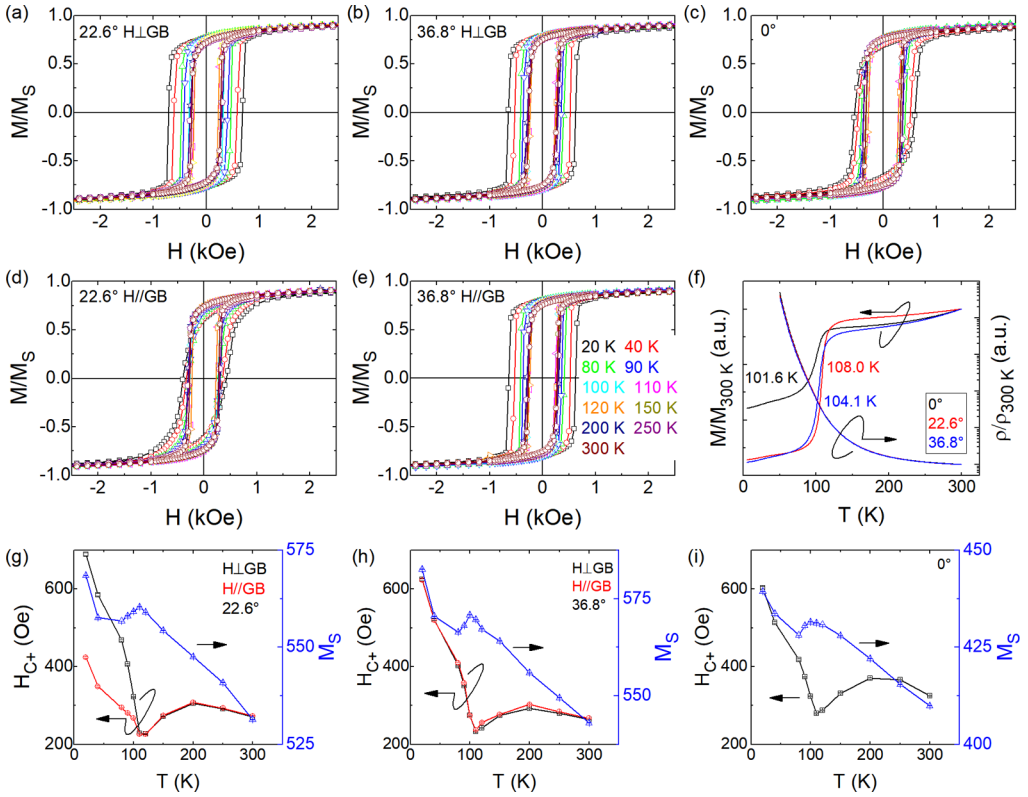

Figure 2. (a–e) Normalized hysteresis loops of Fe_3O_4 films at different temperatures. (f) Temperature dependences of magnetizations and resistivities of Fe_3O_4 films. (g–i) Temperature dependences of coercivities under positive magnetic field (H_{C+}) and saturation magnetizations of Fe_3O_4 films.

have shown that the deviation of GBs from a straight line can already occur at the film/substrate interfaces.[10]

The morphology of the Fe_3O_4 bicrystal film with $\theta = 36.8°$ is shown in the inset of Figure 1e. The Fe_3O_4 film shows no voids in a 10 × 10 μm^2 region (not shown). The straight dark line indicates the GBs. The planar-view HAADF images of the Fe_3O_4 bicrystal film with $\theta = 36.8°$ are shown in Figure 1e,f. By comparing with the 22.6° Fe_3O_4 GBs, the atomic arrangement of Fe_3O_4 at the 36.8° GBs is asymmetric, while the [100] direction of the Fe_3O_4 lattice on both sides is symmetric. The Fe_3O_4 lattice shows a translation along the GBs for about 3.6 Å, which is about 6 times as long for the translation in the $SrTiO_3$ bicrystal with $\theta = 36.8°$.[39] Along the GBs, the atomic arrangement of Fe_3O_4 is short-range-ordered as well. In Figure 1e, some vacancies appear at the GBs marked by white ellipses. The vacancies at GBs resulting in the coordination number reduction may alter the magnetic and electronic properties of Fe_3O_4 bicrystal films (Figure 1f). It should be noted that the GB of the $SrTiO_3$ bicrystal substrate is relatively flat with some steps and shows dislocations.[10,39] Furthermore, the lattice mismatch between Fe_3O_4 and $SrTiO_3$ is about −7.5%. The compress strain in the Fe_3O_4 film can be released by the formation of dislocation. Thus, the atomic structure of Fe_3O_4 along the GBs shows discrepancy.[18]

In order to investigate the effects of GBs on the Fe_3O_4 film, the magnetic properties of Fe_3O_4 films are investigated. Figure 2a–e shows the normalized hysteresis loops of the Fe_3O_4 films on $SrTiO_3$ substrates with and without GBs at the in-plane magnetic field and different temperatures. The magnetizations were recorded up to 50 kOe. The in-plane magnetic field perpendicular (H⊥GB) and parallel (H//GB) to the GB was set during the measurements of the Fe_3O_4 bicrystal films. The Verwey temperatures of 101.6, 108.0, and 104.1 K of Fe_3O_4 films with θ = 0, 22.6°, and 36.8° are determined by the temperature dependences of zero-field cooling magnetizations at a 300-Oe magnetic field (Figure 4f). Above T_V, Fe_3O_4 shows a cubic magnetic anisotropy. The easy axis in the Fe_3O_4 film is along $\langle 100 \rangle_c$.[40,41] The magnetocrystalline anisotropy energy of Fe_3O_4 is equal after an in-plane rotation by 90°. Due to the in-plane rotation of the Fe_3O_4 lattice on bicrystal substrates, the Fe_3O_4 bicrystal films are more difficult to magnetize (Supporting Information, Figure S3). The hysteresis loops of Fe_3O_4 bicrystal films at H⊥GB and H//GB show similar profiles (Supporting Information, Figure S3). Below T_V, the magnetic moments in the Fe_3O_4 film on a single-crystal substrate show an incoherent change (Figure 2c), which suggests a deviation between the easy axis and $\langle 100 \rangle_c$ direction. Magnetic anisotropy investigations show that the in-plane easy axis of Fe_3O_4 films on the $Nb_{0.001}/Sr_{0.999}TiO_3(001)$ single-crystal substrate rotates from $\langle 100 \rangle_c$ to $\langle 110 \rangle_c$ below T_V.[42] Due to the in-plane rotation of the Fe_3O_4 lattice on bicrystal substrates, the angles between $\langle 110 \rangle_c$ and the magnetic field are smaller. Thus, the Fe_3O_4 bicrystal films are easier to magnetize and the hysteresis loops maintain the rectangular profiles (Figure 2a,b,e). Below T_V, the distortion of the Fe_3O_4 lattice from cubic to a monoclinic one has 24 equal manners.[43] Thus, the distribution of $Fe_3O_4[100]_m$ and $[010]_m$ shows the four-fold in-plane symmetry. The Zeeman energies and magnetocrystalline anisotropy energies of the Fe_3O_4 films with H⊥GB and H//GB geometries are identical, which suggests the similar profiles of the hysteresis loops (Figure 2b,e). However, the results of Fe_3O_4 films with θ = 22.6° are

https://dx.doi.org/10.1021/acsami.0c21705
ACS Appl. Mater. Interfaces 2021, 13, 6889–6896

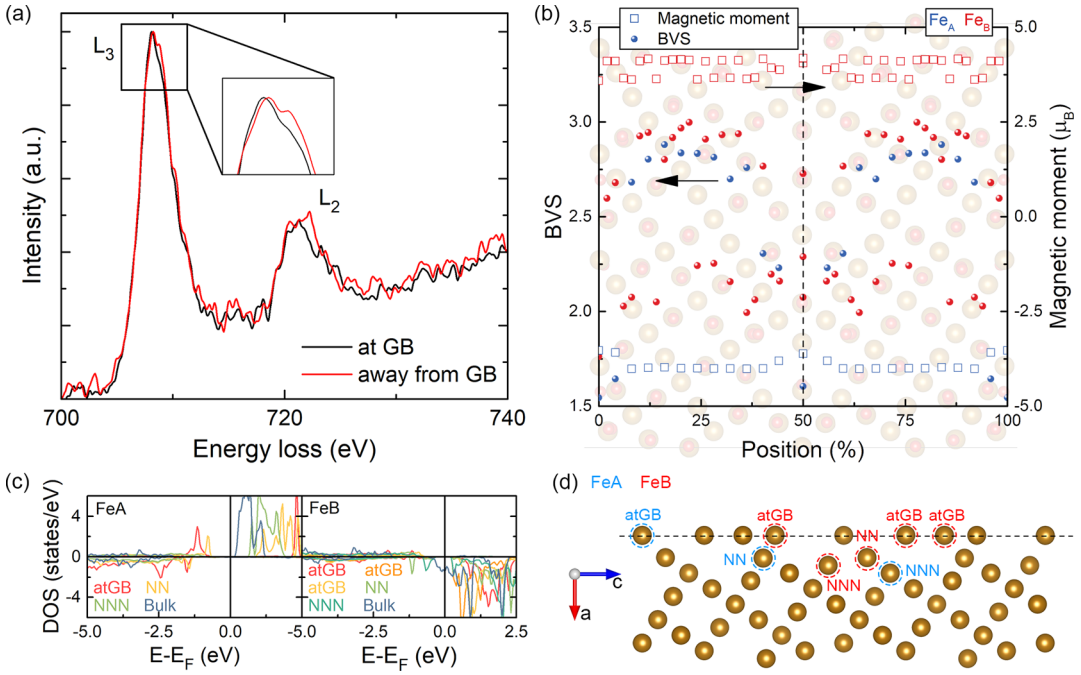

Figure 3. Electronic structures of the Fe_3O_4 bicrystal film with $\theta = 22.6°$. (a) EELS of the Fe $L_{2,3}$-edge at GB and the surrounding grains. (b) BVS and magnetic moments of Fe ions. (c) DOS of the 3d orbital in Fe ions near the GB. The corresponding Fe ions are marked in (d). The dashed lines in (b) and (d) indicate the GB.

not satisfied (Figure 2a,d). The easy axis of the low-temperature phase Fe_3O_4 is along $[001]_m$, which is parallel to the $Fe_3O_4[001]_c$ direction.[40] The strong in-plane magnetic anisotropy in the Fe_3O_4 bicrystal film with $\theta = 22.6°$ suggests a preferred distribution of $Fe_3O_4[001]_m$. The zigzag GB structure alters the local strain which may give rise to the in-plane distribution of $Fe_3O_4[001]_m$. Under $H\perp$GB, the Fe_3O_4 bicrystal film is more easily magnetized. We suppose the angle between $Fe_3O_4[001]_m$ and GB is about 78.7°. In Figure 2f, the temperature-dependent resistivities of Fe_3O_4 films were measured with the decrease of temperature. The Verwey temperatures where $\partial^2 \log \rho / \partial T^2 = 0$ determined by $\rho-T$ curves of Fe_3O_4 films with θ = 0°, 22.6°, and 36.8° are 97.9, 100.9, and 98.9 K, respectively. The thinner thickness of Fe_3O_4 films and dislocation resulting from the release of lattice strain leads to the broadening of Verwey transition and the decrease of T_V comparing to bulk Fe_3O_4.[18] The different temperature-changing processes result in the discrepant T_V because of the essence of first-order phase transition.[31] Different methods suggest that the Fe_3O_4 bicrystal films exhibit a higher transition temperature.

Figure 2g–i shows the temperature-dependent coercivity and saturation magnetization of Fe_3O_4 films. Above T_V, the coercivity of the Fe_3O_4 film without GBs is larger than that of Fe_3O_4 bicrystal films. With the decrease of temperature, the coercivity of Fe_3O_4 films increases, which shows the local maxima at 200 K. Below 200 K, the coercivity reduces and shows the local minima at T_V due to the reduction of magnetocrystalline anisotropy constant and magnetic isotropy.[40] The saturation magnetization of Fe_3O_4 films increases with the decrease of temperature and shows the local maxima at T_V.[40] Below T_V, the establishment of uniaxial magnetic anisotropy in Fe_3O_4 causes the increase of coercivity. The temperature-dependent coercivities in Fe_3O_4 films with θ = 0° and 36.8° are similar. However, the Fe_3O_4 film with θ = 22.6° shows a larger (smaller) coercivity with $H\perp$GB (H//GB) geometries due to the preferred easy axis distribution. The saturation magnetizations of Fe_3O_4 films show reduction below T_V. The formation of twin boundaries resulting from the different distortion manners of monoclinic Fe_3O_4 lattice below T_V introduces antiferromagnetic coupling between Fe_B ions and decreases the saturation magnetizations.[26,43] Although the temperature-dependent saturation magnetizations of Fe_3O_4 films are similar, the saturation magnetizations of Fe_3O_4 bicrystal films are enhanced. APBs and spin crossover have an impact on the magnetic properties of Fe_3O_4. However, these factors decrease the magnetization of the Fe_3O_4 film.[18,44] Furthermore, the coincident fabrication condition results in a similar density of APBs, which can rule out the impact from APBs. It should be noted that the saturation magnetizations of Fe_3O_4 films show an anomalous increase below 40 K. The KAPTON tape used to fix the sample shows a strong magnetization at low temperatures (Supporting Information, Figure S4), which enhances the total magnetic moments.

In order to reveal the distinctive magnetic properties of Fe_3O_4 bicrystal films, the electronic structure of Fe_3O_4 at GBs is investigated. In the Fe_3O_4 bicrystal film with $\theta = 22.6°$, the electronic structure at the symmetric GB is determined by high spatial resolution electron energy loss spectroscopy (EELS) (Figure 3a). The intensity of the Fe L_2-edge shows no obvious change across the GBs, while the Fe L_2-edge shifts to low energy. The fine structure of the Fe L_3-edge is different between the GB and surrounding grains, wherein the intensities of the L_3-edge main crests' shoulders deriving from Fe_A^{3+} decrease at GBs, indicating the reduction of the Fe^{3+}/Fe^{2+} ratio.[45] The detailed EELS results across GBs and the corresponding scanning area are shown in Supporting Information, Figure S2b. DFT calculations show similar results at GBs in Fe_3O_4 bicrystal films. Figure 3b shows the magnetic moments and valence states of Fe ions at the symmetric GB

https://dx.doi.org/10.1021/acsami.0c21705
ACS Appl. Mater. Interfaces 2021, 13, 6889–6896

with $\theta = 22.6°$. The calculation model is shown in Figure 1d. The valence states of Fe and O ions are calculated through the method of bond-valence-sum (BVS). Here, BVS for a single ion has an expression as

$$\mathrm{BVS} = \sum_{i}^{n} \exp\left(\frac{R_0 - R_i}{b}\right)$$

where R_0 is the bond−valence parameter, R_i refers to the ith bond length, and $b = 0.37$ Å.[46] The fluctuated valences of the Fe_B ions indicate the appearance of charge ordering (Figure 3b). The reduced valence states of Fe_A^{3+} at GBs are in accord with the EELS results. In addition, the valence states of Fe_B^{3+} at GB show reduction as well. The average valence of Fe_A (Fe_B) ions of +2.47 (+2.50) is lower (higher) than the bulk of +2.73 (+2.49). The magnetic moments of Fe_A ions are reduced by ∼0.4 μ_B at GBs. The Fe_B magnetic moments at GBs are almost unchanged. The net magnetic moments of ferrimagnetic Fe_3O_4 derive from Fe_B ions. Hence, the total magnetic moments of Fe_3O_4 increase, which is reflected by the enhancement of saturation magnetizations in Fe_3O_4 bicrystal films.

Figure 3c shows the density of states (DOS) of 3d electrons in Fe ions at GBs with $\theta = 22.6°$. The symmetric ions on both sides are equal due to the symmetric structure across GBs. We thus only show the DOS results of one side. With the increased distance between Fe ions and the GB, Fe ions can be classified as at GB (atGB), the nearest neighbor (NN), and the next-nearest neighbor (NNN). The corresponding distribution of Fe ions is shown in Figure 3d. In the left panel of Figure 3c, the spin-up bands of Fe_A ions at GBs are occupied by extra electronic states. With the increase of the distance to the GB, the extra electronic states on spin-up band in Fe_A ions gradually reduce to a bulk value, while the electronic states on the spin-down band in Fe_A ions gradually localize in the deep energy level. The average Fe_A-O bond length of 1.99 Å at GBs is larger than that of the bulk of 1.90 Å, whereas the average bond length of 2.05 Å for Fe_B−O is similar to the cubic one of 2.08 Å. The elongated Fe_A-O bonds at GBs weaken the charge transfer between Fe_A and O ions, which results in the occupied electronic states on the spin-up 3d band of Fe_A ions and further reduces the magnetic moments and valence states of the Fe_A ions. In the right panel of Figure 3c, a band gap larger than 0.27 eV opens at the Fermi level in Fe_B ions around the GB. However, the Fe_B ion in bulk Fe_3O_4 shows half-metallicity. By comparing with the Fe_B ions in cubic Fe_3O_4, 3d electrons in the spin-down band are almost unoccupied in Fe ions at GB. However, in the NN and NNN Fe ions, the spin-down 3d electrons are localized. The DOS results suggest the essence of charge ordering at Fe_B sites, which is in accord with BVS results. The charge ordering is familiar in the low-temperature phase Fe_3O_4.[29,30,47] Calculation results have shown that the breakdown of cubic symmetry in Fe_3O_4 results in the opening of a band gap of about 0.2 eV at the Fermi level.[48] The broken cubic symmetry of Fe_3O_4 at GBs distorts the O-octahedral around Fe_B ions and leads to the appearance of charge ordering and band gap. In the low-temperature phase Fe_3O_4, a larger band gap results in a higher transition temperature.[49] The maintained band gap and charge ordering in Fe_3O_4 bicrystal films may also delay the Verwey transition and lead to a higher T_V in Fe_3O_4 bicrystal films.

For the case of $\theta = 36.8°$, two calculation models marked as M_{36A} and M_{36B} are built based on the TEM results. Figure 4a shows the layer-resolved DOS of 3d electrons of Fe_A and Fe_B ions near GBs in M_{36A}. DOS results of the symmetric Fe_A layers are similar. The reduction of neighboring ions and the increased Fe_A-O bond length at GBs cause the reduction of electron transfer between Fe_A and O ions, resulting in the occupation of spin-up 3d electrons in the Fe_A ions. The extra occupied electronic states decrease the magnetic moments and valence states of the Fe_A ions. With the increase of the distance to GBs, the extra spin-up 3d electronic states reduce to bulk value and the spin-down 3d electrons in Fe_A ions gradually localize in the deep energy level. For Fe_B ions, a band gap of 0.27 eV opens at the Fermi level (Figure 4a). The spin-down 3d electrons show the localization in some Fe_B ions, that is, charge ordering. Figure 4b shows the valence states and magnetic moments of Fe ions in M_{36A}. The valence states of the Fe ions reduce at GBs. Although the magnetic moments of Fe_A and Fe_B ions reduce at GBs, the total magnetic moments in M_{36A} are enhanced. Thus, the Fe_3O_4 bicrystal film shows a larger saturation magnetization. The fluctuated Fe_B valence states are in line with the DOS results. In Supporting Information, Figure S5, the layer-resolved DOS results of Fe ions in M_{36B} are similar. The magnetic moments and valence states of Fe ions at GBs in M_{36B} are smaller than those of M_{36A}, stemming from the Fe and O vacancies at GBs as shown in Figure 1f.

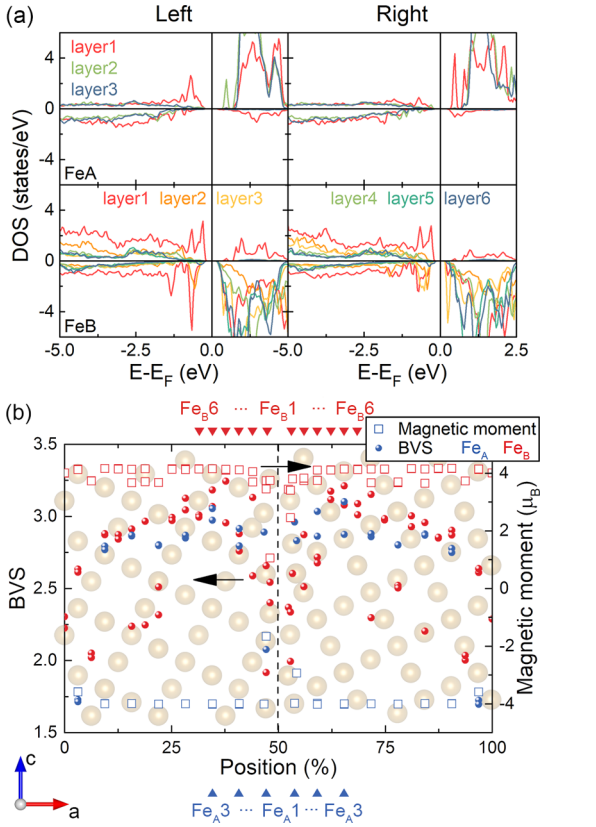

Figure 4. (a) Layer-resolved DOS on 3d orbitals of Fe_A and Fe_B ions in M_{36A}. (b) BVS and magnetic moments of Fe ions. Fe ions in specific layers are marked in (b). The dashed line in (b) indicates the GB.

DFT results manifest that the break of cubic symmetry in Fe_3O_4 bicrystal films introduces the changes of magnetizations and electronic structures. In order to determine the effects of GBs on the transport properties, MR of Fe_3O_4 films under in-

https://dx.doi.org/10.1021/acsami.0c21705
ACS Appl. Mater. Interfaces 2021, 13, 6889−6896

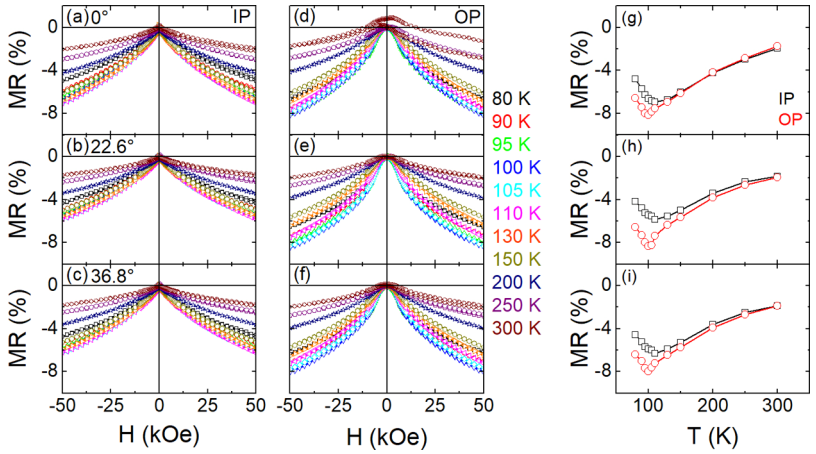

Figure 5. MR behavior of Fe_3O_4 films with (a–c) IP and (d–f) OP geometries. (g–i) Temperature dependences of MR in Fe_3O_4 films with IP and OP configurations under 50 kOe magnetic field. Upper, middle, and lower panels are the MR results of Fe_3O_4 films with θ = 0, 22.6, and 36.8°, respectively.

plane (IP) and out-of-plane (OP) magnetic field and $I-V$ characteristics are measured. The $I-V$ curves of Fe_3O_4 films show linear profiles without rectification in the temperature range from 80 to 300 K (not shown). The MR in this work is defined as MR = $(R_H - R_0)/R_0 \times 100\%$, where R_H and R_0 are the resistances under a given magnetic field of H and zero magnetic field. The direction of the magnetic field is perpendicular to the current during the measurements so that the AMR effect from Lorentz force can be ruled out. Figure 5a–f shows the magnetic field-dependent MR of Fe_3O_4 films with θ = 0, 22.6, and 36.8°. With IP configuration, the MR curves show two peaks at the coercive fields. In order to clarify the MR mechanism at different temperatures, the normalized MR curves are plotted in Supporting Information, Figure S6a–c. The similar profiles of normalized MR curves indicate a consistent mechanism of MR. Based on the model proposed by Eerenstein et al., the dependence of MR on the magnetic field can be expressed as

$$\mathrm{MR} = -C\left[\frac{M_S\mu_0 H}{W_{AF}} - \left(\frac{M_S\mu_0 H}{W_{AF}}\right)^{3/2}\right] \quad (1)$$

where C only depends on the density of antiferromagnetic scattering centers including APBs and twin boundaries formed below T_V.[21,26] M_S is the saturation magnetization. $W_{AF} = {A_{AF}}^2/A_F d^2$, where A_F is the bulk ferromagnetic exchange stiffness, A_{AF} is the antiferromagnetic exchange stiffness across APBs and twin boundaries, and d is the distance between the two magnetic moments.[21,50] In the temperature range from 80 to 300 K, MR curves of the Fe_3O_4 films can be reproduced by fittings with eq 1 (Supporting Information, Figure S6d–f), which manifests that the MR in Fe_3O_4 films is dominated by the spin-dependent transport across APBs and twin boundaries.[21,26,50,51] Fitting results show that the parameter of C in Fe_3O_4 films with θ = 0° is slightly larger (Supporting Information, Figure S6g–i). With the decrease of temperature, the magnitudes of C show the local maximum at 110 K (Supporting Information, Figure S6g–i), where the magnitudes of MR with IP geometry show the local maximum (Figure 5g–i). The temperature-dependent MR of a Fe_3O_4 single crystal and thicker films on MgO ($SrTiO_3$) substrates show a peak value near T_V, which is different from the results in this work.[24–26,52] Gridin et al. have shown that the magnitude of MR at T_V is inversely proportional to the full width at half-maximum of the MR peak.[52] The broadened Verwey transition deriving from the compressed strain and smaller thickness in this work may lead to the absent MR peak. With OP configuration, MR curves show a quadratic behavior up to 5 kOe due to the competition between the anisotropy energy and Zeeman energy (Figure 5d–f).[21] Below 110 K, Fe_3O_4 films exhibit a larger MR with OP configuration by comparing the results with IP geometry, which suggests the anisotropic MR (AMR) effects (Figure 5g–i). Below T_V, the magnetocrystalline anisotropy constant is about 10 times greater than that above T_V.[18] Together with the demagnetization under OP magnetic field, Fe_3O_4 exhibits more significant MR. The weakened magnetic anisotropy of Fe_3O_4 above T_V results in the reduction of AMR in the Fe_3O_4 film without GBs (Figure 5g).[40] However, the Fe_3O_4 bicrystal films exhibit more conspicuous AMR above T_V. The discrepant $\langle 100\rangle_c$ at GB in Fe_3O_4 bicrystal films alters the magnetocrystalline anisotropy, which enhances the magnitude of AMR even above T_V (Figure 5g–i). With the increase of temperature, the magnitudes of MR with OP configuration show the local maximum at 100 K, which is lower than the temperature with IP configuration. The different temperature where MR shows local maxima may result from the magnetic isotropy of Fe_3O_4, which occurs at a higher temperature.[40] With IP configuration, the magnetic isotropy enhances the magnitude of MR and shifts the maximum of MR to a higher temperature.[26] However, the effect of magnetic isotropy is suppressed with OP geometry due to the demagnetization field in Fe_3O_4 films. Thus, the local maximum of MR appears at a lower temperature.

The magnetic and transport properties are measured in another Fe_3O_4 bicrystal film with θ = 14.3° in order to examine the effect of GB on the magnetic and transport properties. The Fe_3O_4 bicrystal film shows a strong in-plane magnetic anisotropy below T_V, which is similar to the results of films with θ = 22.6° (Supporting Information, Figure S7a,b). The Verwey temperature for the Fe_3O_4 bicrystal film of 108.5 K is higher than for the Fe_3O_4 film without GBs (Supporting Information, Figure S7c). Due to the strong in-plane magnetic anisotropy, the coercivity shows the deviation at different magnetic field directions below T_V (Supporting Information,

https://dx.doi.org/10.1021/acsami.0c21705
ACS Appl. Mater. Interfaces 2021, 13, 6889–6896

Figure S7d). The MR behavior shows the similar magnetic field and temperature dependences (Supporting Information, Figure S8). Due to the introduction of GB, the AMR effect is more conspicuous above T_V, which is similar to the results in other Fe_3O_4 bicrystal films (Supporting Information, Figure S8c).

4. CONCLUSIONS

In summary, the atomic structure, magnetic, and transport properties of Fe_3O_4 bicrystal films were investigated. The distinctive lattice structure at GBs elongates the Fe_A-O bond length, resulting in the reduction of the charge transfer and magnetization enhancement of the Fe_3O_4 bicrystal films. The break of cubic symmetry at GBs leads to the band gap opening and charge ordering, which shifts the Verwey transition to a higher temperature. Due to the macroscopic rotation of the Fe_3O_4 lattice on bicrystal substrates, the magnetic anisotropy is altered, which leads to a more conspicuous AMR in the Fe_3O_4 bicrystal films from 80 to 300 K. The magnetic and electronic properties are altered in half-metallic Fe_3O_4 films by the introduction of GBs, which may be helpful to the defect-based spintronic devices.

■ ASSOCIATED CONTENT

Supporting Information

The Supporting Information is available free of charge at https://pubs.acs.org/doi/10.1021/acsami.0c21705.

> XRD result of the $Fe_3O_4/SrTiO_3$ film with $\theta = 0°$, additional TEM and EELS results of Fe_3O_4 bicrystal films with $\theta = 22.6°$, normalized hysteresis loops of Fe_3O_4 films at 20 and 300 K, temperature-dependent magnetization of KAPTON tape, electronic structures, BVS and magnetic moments of Fe ions in M_{36B}, fitting results of MR in Fe_3O_4 films, and magnetic properties and MR of the Fe_3O_4 film with $\theta = 14.3°$ (PDF)

■ AUTHOR INFORMATION

Corresponding Authors

Peng Gao − *International Center for Quantum Materials, School of Physics and Electron Microscopy Laboratory, School of Physics, Peking University, Beijing 100871, China; Collaborative Innovation Center of Quantum Matter, Beijing 100871, China;* orcid.org/0000-0003-0860-5525; Email: p-gao@pku.edu.cn

Wenbo Mi − *Tianjin Key Laboratory of Low Dimensional Materials Physics and Processing Technology, School of Science, Tianjin University, Tianjin 300354, China;* orcid.org/0000-0002-9108-9930; Email: miwenbo@tju.edu.cn

Authors

Xiang Liu − *Tianjin Key Laboratory of Low Dimensional Materials Physics and Processing Technology, School of Science, Tianjin University, Tianjin 300354, China*

Mei Wu − *International Center for Quantum Materials, School of Physics, Peking University, Beijing 100871, China*

Ke Qu − *Electron Microscopy Laboratory, School of Physics, Peking University, Beijing 100871, China*

Complete contact information is available at: https://pubs.acs.org/10.1021/acsami.0c21705

Author Contributions

⊥X.L.and M.W. contribute equally.

Notes

The authors declare no competing financial interest.

■ ACKNOWLEDGMENTS

This work was supported by the National Key R&D Program of China (2016YFA0300804) and the National Natural Science Foundation of China (U1632152 and 51871161, 51672007, and 11974023). P.G. also acknowledges the support of the Key R&D Program of Guangdong Province (2018B030327001, 2018B010109009).

■ REFERENCES

(1) Alloul, H.; Bobroff, J.; Gabay, M.; Hirschfeld, P. J. Defects in Correlated Metals and Superconductors. *Rev. Mod. Phys.* **2009**, *81*, 45−108.

(2) Sun, C. P.; Balluffi, R. W. Secondary Grain Boundary Dislocations in [001] Twist Boundaries in MgO I. Intrinsic Structures. *Philos. Mag. A* **1982**, *46*, 49−62.

(3) Morrissey, K. J.; Carter, C. B. Faceted Grain Boundaries in Al_2O_3. *J. Am. Ceram. Soc.* **1984**, *67*, 292−301.

(4) Merkle, K. L.; Smith, D. J. Atomic Resolution Electron Microscopy of NiO Grain Boundaries. *Ultramicroscopy* **1987**, *22*, 57−70.

(5) Merkle, K. L.; Smith, D. J. Atomic Structure of Symmetric Tilt Grain Boundaries in NiO. *Phys. Rev. Lett.* **1987**, *59*, 2887−2890.

(6) Gunnarsson, R.; Hanson, M. Magnetization Reversal Processes in Magnetic Bicrystal Junctions. *Phys. Rev. B: Condens. Matter Mater. Phys.* **2006**, *73*, 014435.

(7) Gunnarsson, R.; Kadigrobov, A.; Ivanov, Z. Model for Spin-Polarized Transport in Perovskite Manganite Bicrystal Grain Boundaries. *Phys. Rev. B: Condens. Matter Mater. Phys.* **2002**, *66*, 024404.

(8) Khare, N.; Moharil, U. P.; Gupta, A. K.; Raychaudhuri, A. K.; Pai, S. P.; Pinto, R. Temperature Dependence of Magnetoresistance and Nonlinear Conductance of the Bicrystal Grain Boundary in Epitaxial $La_{0.67}Ba_{0.33}MnO_3$ Thin Films. *Appl. Phys. Lett.* **2002**, *81*, 325−327.

(9) Dimos, D.; Chaudhari, P.; Mannhart, J. Superconducting Transport Properties of Grain Boundaries in $YBa_2Cu_3O_7$ Bicrystals. *Phys. Rev. B: Condens. Matter Mater. Phys.* **1990**, *41*, 4038−4049.

(10) Traeholt, C.; Wen, J. G.; Zandbergen, H. W.; Shen, Y.; Hilgenkamp, J. W. M. TEM Investigation of $YBa_2Cu_3O_7$ Thin Films on $SrTiO_3$ Bicrystals. *Phys. C Supercond.* **1994**, *230*, 425−434.

(11) Cardona, A. H.; Suzuki, H.; Yamashita, T.; Young, K. H. Transport Characteristics of $Tl_2Ba_2CaCu_2O_8$ Bicrystal Grain Boundary Junctions at 77 K. *Appl. Phys. Lett.* **1994**, *62*, 411−413.

(12) Gao, P.; Yang, S. Z.; Ishikawa, R.; Li, N.; Feng, B.; Kumamoto, A.; Shibata, N.; Yu, P.; Ikuhara, Y. Atomic-Scale Measurement of Flexoelectric Polarization at $SrTiO_3$ Dislocations. *Phys. Rev. Lett.* **2018**, *120*, 267601.

(13) Li, X.; Yin, L.; Lai, Z.; Wu, M.; Sheng, Y.; Zhang, L.; Sun, Y.; Chen, S.; Li, X.; Zhang, J.; Li, Y.; Liu, K.; Wang, K.; Yu, D.; Bai, X.; Mi, W.; Gao, P. Atomic Origin of Spin-Valve Magnetoresistance at the $SrRuO_3$ Grain Boundary. *Natl. Sci. Rev.* **2020**, *7*, 755−762.

(14) Néel, M. L. Propriétés magnétiques des ferrites ; ferrimagnétisme et antiferromagnétisme. *Ann. Phys.* **1948**, *12*, 137−198.

(15) Yanase, A.; Siratori, K. Band Structure in the High Temperature Phase of Fe_3O_4. *J. Phys. Soc. Jpn.* **1984**, *53*, 312−317.

(16) Jeng, H. T.; Guo, G. Y. First-Principles Investigations of the Electronic Structure and Magnetocrystalline Anisotropy in Strained Magnetite Fe_3O_4. *Phys. Rev. B: Condens. Matter Mater. Phys.* **2002**, *65*, 094429.

(17) Wright, J. P.; Attfield, J. P.; Radaelli, P. G. Charge Ordered Structure of Magnetite Fe_3O_4 below the Verwey Transition. *Phys. Rev. B: Condens. Matter Mater. Phys.* **2002**, *66*, 214422.
(18) Liu, X. H.; Liu, W.; Zhang, Z. D. Evolution of Magnetite Properties in the Vicinity of the Verwey Transition in Fe_3O_4 Thin Films. *Phys. Rev. B* **2017**, *96*, 094405.
(19) Liu, X.; Mi, W. B. Spontaneous Ferroelectricity in Strained Low-Temperature Monoclinic Fe_3O_4: A first-Principles Study. *Front. Physiol.* **2018**, *13*, 134204.
(20) Margulies, D. T.; Parker, F. T.; Rudee, M. L.; Spada, F. E.; Chapman, J. N.; Aitchison, P. R.; Berkowitz, A. E. Origin of the Anomalous Magnetic Behavior in Single Crystal Fe_3O_4 Films. *Phys. Rev. Lett.* **1997**, *79*, 5162−5165.
(21) Eerenstein, W.; Palstra, T. T. M.; Saxena, S. S.; Hibma, T. Spin-Polarized Transport across Sharp Antiferromagnetic Boundaries. *Phys. Rev. Lett.* **2002**, *88*, 247204.
(22) Celotto, S.; Eerenstein, W.; Hibma, T. Characterization of Anti-Phase Boundaries in Epitaxial Magnetite Films. *Eur. Phys. J. B* **2003**, *36*, 271−279.
(23) Mckenna, K. P.; Hofer, F.; Gilks, D.; Lazarov, V. K.; Chen, C. L.; Wang, Z. C.; Ikuhara, Y. Atomic-Scale Structure and Properties of Highly Stable Antiphase Boundary Defects in Fe_3O_4. *Nat. Commun.* **2014**, *5*, 5740.
(24) Gong, G. Q.; Gupta, A.; Xiao, G.; Qian, W.; Dravid, V. P. Magnetoresistance and Magnetic Properties of Epitaxial Magnetite Thin Films. *Phys. Rev. B: Condens. Matter Mater. Phys.* **1997**, *56*, 5096−5099.
(25) Ziese, M.; Blythe, H. J. Magnetoresistance of Magnetite. *J. Phys.: Condens. Matter* **2000**, *12*, 13−28.
(26) Liu, X.; Mi, W.; Zhang, Q.; Zhang, X. Magnetoresistance of Epitaxial and Polycrystalline Fe_3O_4 Films near Verwey Transition. *Appl. Phys. Lett.* **2018**, *113*, 012401.
(27) Verwey, E. J. W. Electronic Conduction of Magnetite (Fe_3O_4) and its Transition Point at Low Temperatures. *Nature* **1939**, *144*, 327−328.
(28) Verwey, E. J. W.; Haayman, P. W. Electronic Conductivity and Transition Point of Magnetite ("Fe_3O_4"). *Physica* **1941**, *8*, 979−987.
(29) Verwey, E. J. W.; Heilmann, E. L. Physical Properties and Cation Arrangement of Oxides with Spinel Structures I. Cation Arrangement in Spinels. *J. Chem. Phys.* **1947**, *15*, 174−180.
(30) Verwey, E. J.; Haayman, P. W.; Romeijn, F. C. Physical Properties and Cation Arrangement of Oxides with Spinel Structures II. Electronic Conductivity. *J. Chem. Phys.* **1947**, *15*, 181−187.
(31) Liu, X. H.; Rata, A. D.; Chang, C. F.; Komarek, A. C.; Tjeng, L. H. Verwey Transition in Fe_3O_4 Thin Films: Influence of Oxygen Stoichiometry and Substrate-Induced Microstructure. *Phys. Rev. B: Condens. Matter Mater. Phys.* **2014**, *90*, 125142.
(32) Liu, X. H.; Chang, C. F.; Rata, A. D.; Komarek, A. C.; Tjeng, L. H. Fe_3O_4 Thin Films: Controlling and Manipulating an Elusive Quantum Material. *npj Quantum Mater.* **2016**, *1*, 16027.
(33) Kresse, G.; Furthmüller, J. Efficient Iterative Schemes for Ab Initio Total-Energy Calculations Using a Plane-Wave Basis Set. *Phys. Rev. B: Condens. Matter Mater. Phys.* **1996**, *54*, 11169−11186.
(34) Blöchl, P. E. Projector Augmented-Wave Method. *Phys. Rev. B: Condens. Matter Mater. Phys.* **1994**, *50*, 17953−17979.
(35) Anisimov, V. I.; Zaanen, J.; Andersen, O. K. Band Theory and Mott Insulators: Hubbard *U* Instead of Stoner I. *Phys. Rev. B: Condens. Matter Mater. Phys.* **1991**, *44*, 943−954.
(36) Perdew, J. P.; Wang, Y. Accurate and Simple Analytic Representation of the Electron-Gas Correlation Energy. *Phys. Rev. B: Condens. Matter Mater. Phys.* **1992**, *45*, 13244−13249.
(37) Liechtenstein, A. I.; Anisimov, V. I.; Zaanen, J. Density-Functional Theory and Strong Interactions: Orbital Ordering in Mott-Hubbard Insulators. *Phys. Rev. B: Condens. Matter Mater. Phys.* **1995**, *52*, 5467−5470.
(38) Jeng, H. T.; Guo, G. Y.; Huang, D. J. Charge-Orbital Ordering in Low-Temperature Structures of Magnetite: GGA+*U* Investigations. *Phys. Rev. B: Condens. Matter Mater. Phys.* **2006**, *74*, 195115.
(39) Ravikumar, V.; Dravid, V. P. Atomic Structure of Undoped Σ=5 Symmetrical Tilt Grain Boundary in Strontium Titanate. *Ultramicroscopy* **1993**, *52*, 557−563.
(40) Bickford, L. R., Jr. Ferromagnetic Resonance Absorption in Magnetite Single Crystals. *Phys. Rev.* **1950**, *78*, 449−457.
(41) Cuñado, J. L. F.; Camarero, J.; Pedrosa, F. J.; Nemes, N. M.; Sanz, M.; Oujja, M.; Rebollar, E.; Marco, J. F.; de la Figuera, J.; Monti, M.; Castillejo, M.; Feher, T.; Nafradi, B.; Forró, L.; Bollero, A. Evidence of Anomalous Switching of the In-Plane Magnetic Easy Axis with Temperature in Fe_3O_4 Film on $SrTiO_3$:Nb by v-MOKE and Ferromagnetic Resonance. *Nanoscale* **2019**, *11*, 19870−19876.
(42) Kasama, T.; Church, N. S.; Feinberg, J. M.; Dunin-Borkowski, R. E.; Harrison, R. J. Direct Observation of Ferrimagnetic/Ferroelastic Domain Interactions in Magnetite below the Verwey Transition. *Earth Planet. Sci. Lett.* **2010**, *297*, 10−17.
(43) Chen, C.; Li, H.; Seki, T.; Yin, D.; Sanchez-Santolino, G.; Inoue, K.; Shibata, N.; Ikuhara, Y. Direct Determination of Atomic Structure and Magnetic Coupling of Magnetite Twin Boundaries. *ACS Nano* **2018**, *12*, 2662−2668.
(44) Yazdi, M. B.; Major, M.; Wildes, A.; Wilhelm, F.; Rogalev, A.; Donner, W.; Alff, L. Possible Evidence for a Spin-State Crossover in the Verwey State in Fe_3O_4 Thin Films. *Phys. Rev. B* **2016**, *93*, 014439.
(45) Calmels, L.; Rusz, J. Momentum-Resolved EELS and EMCD Spectra from the Atomic Multiplet Theory: Application to Magnetite. *Ultramicroscopy* **2010**, *110*, 1042−1045.
(46) Brese, N. E.; O'keeffe, M. Bond-Valence Parameters for Solids. *Acta Crystallogr. Sect. B Struct. Sci.* **1991**, *47*, 192−197.
(47) Senn, M. S.; Wright, J. P.; Attfield, J. P. Charge Order and Three-Site Distortions in the Verwey Structure of Magnetite. *Nature* **2012**, *481*, 173−176.
(48) Liu, H.; Di Valentin, C. Band Gap in Magnetite above Verwey Temperature Induced by Symmetry Breaking. *J. Phys. Chem. C* **2017**, *121*, 25736−25742.
(49) Liu, X.; Yin, L.; Mi, W. B. Biaxial Strain Effect Induced Electronic Structure Alternation and Trimeron Recombination in Fe_3O_4. *Sci. Rep.* **2017**, *7*, 43403.
(50) Ramos, A. V.; Moussy, J.-B.; Guittet, M.-J.; Bataille, A. M.; Gautier-Soyer, M.; Viret, M.; Gatel, C.; Bayle-Guillemaud, P.; Snoeck, E. Magnetotransport Properties of Fe_3O_4 Epitaxial Thin Films: Thickness Effects Driven by Antiphase Boundaries. *J. Appl. Phys.* **2006**, *100*, 103902.
(51) Sofin, R. G. S.; Arora, S. K.; Shvets, I. V. Positive Antiphase Boundary Domain Wall Magnetoresistance in Fe_3O_4(110) Hetero-epitaxial Films. *Phys. Rev. B: Condens. Matter Mater. Phys.* **2011**, *83*, 134436.
(52) Gridin, V. V.; Hearne, G. R.; Honig, J. M. Magnetoresistance Extremum at the First-Order Verwey Transition in Magnetite (Fe_3O_4). *Phys. Rev. B: Condens. Matter Mater. Phys.* **1996**, *53*, 15518−15521.

https://dx.doi.org/10.1021/acsami.0c21705
ACS Appl. Mater. Interfaces 2021, 13, 6889−6896